Composition of ore-forming fluids in the Huangshuian carbonatite-related Mo-(REE) deposit: Insights from LA-ICP-MS analyses of fluid inclusions

Wei Zhang [a], Hua-Kai Chen [b], Jing-Hui Li [b], Wei Terry Chen [a,c,*], Xing-Chun Zhang [a], Yan-Wen Tang [a]

[a] *State Key Laboratory of Ore Deposit Geochemistry, Institute of Geochemistry Chinese Academy of Sciences, Guiyang 550081, China*
[b] *Henan Nuclear Geological Bureau, Zhengzhou 450044, China*
[c] *University of Chinese Academy of Sciences, Beijing, 10039, China*

A B S T R A C T

The carbonatites in the southern margin of the North China Craton are distinguishable by containing abundant quartz and are closely spatially associated with Mo-(REE) deposits. Unveiling the nature of ore-forming fluids is key to understand the genesis of these Mo-(REE) deposits and to explore their potential genetic relationships with the quartz-rich carbonatites, but such issues were currently not convincingly addressed. Here, we provide detailed petrographic, microthermometric and LA-ICP-MS analyses of the fluid inclusions hosted in the primary quartz from the carbonatites in the Huangshuian Mo-(REE) deposit which is the largest Mo-(REE) one in the region, containing 0.4 million tons of Mo metal with REEs as the major by-product. Our results show that the fluid inclusions in the quartz of the carbonatites are two- and three-phase CO_2-bearing types with high homogenization temperatures (average at 396 °C) and low salinities (average at 3.88 wt% NaCl equiv). The LA-ICP-MS analyses of these inclusions reveal that the primary fluids contain high concentrations of La, Ce, Pr, Nd, Sr, and Ba, similar to typical carbonatite-related fluids. In addition, they are characterized by high Y, Cu, Pb, and Zn. Such a metal association is broadly consistent with the mineral assemblages of the Huangshuian Mo-(REE) deposit, such as the widespread barite, bastnäsite, xenotime, chalcopyrite, galena, and sphalerite, strongly supporting the close genetic relation of the deposit with the quartz-rich carbonatites. Although the concentrations of Mo are extremely low in these inclusions (below the detect limit), it was constrained to be gradually enriched in evolved fluids. Considering that the recorded fluids in quartz represent earliest generation of fluids exsolved from carbonatite magmas, our new results highlight that quantifying metal budgets of fluid inclusions could be a robust way to evaluate fertility of carbonatites that are widespread in the southern margin of the North China Craton.

1. Introduction

Carbonatites are defined by the International Union of Geological Sciences (IUGS) as igneous rocks composed of more than 50 modal percent carbonate and less than 20 wt% SiO_2 (Le Maitre, 2002). Although volumetrically rare compared to silicate igneous rocks, carbonatites are important exploration targets as they are generally associated with REE mineralization and are also important source of Nb, P, Cu and fluorite (Groves and Gwalani, 2004; Verplanck et al., 2016; Simandl and Paradis, 2018). Typical carbonatite-related deposits include the Bayan Obo Fe-REE-Nb deposit in China (Yang et al, 2011; Fan et al., 2016), Mountain Pass REE deposit in USA (Castor, 2008),

Phalaborwa Cu deposit in South Africa (Milani et al., 2017), Amba Dongar fluorite deposit in India (Palmer and Williams-Jones, 1996) and Matongo P deposit in Burundi (Decrée et al., 2016).

The carbonatites in the southern margin of the North China Craton (S-NCC) are unique for containing abundant quartz and spatially associated with Mo-(REE)-rich hydrothermal veins constituting several Mo-(REE) deposits (Xu et al., 2010; Song et al., 2015, 2016; Zhang et al., 2019). Similar carbonatite-associated Mo-(REE) deposits were not documented in other places worldwide, and thus the ore genesis and possible genetic relationships of Mo-(REE) ores with the Si-rich carbonatite have long been attractive topics but currently are still not clearly addressed. Unveiling the nature and source of the ore-forming fluids is

the key to resolve these issues. However, such kind of work was not available in previous studies which mainly focused on geochemical and isotopic features of the carbonatites and ores (e.g., Xu et al., 2007, 2010, 2011; Cao et al., 2014; Song et al., 2015, 2016; Bai et al., 2019).

Fluid inclusions in magmatic-hydrothermal deposits are invaluable samples of paleohydrothermal fluids responsible for ore formation (Roedder, 1984). Recent development of laser ablation-inductively coupled plasma-mass spectrometry (LA-ICP-MS) allows precisely quantifying the composition of single fluid inclusion (Heinrich et al., 2003). Such in-situ method is advantaged by avoiding the mixture of signals from multiple fluid generations (Heinrich et al., 2003; Pettke et al., 2012). Therefore, LA-ICP-MS analyses of fluid inclusions have been widely used to constrain the nature and source of ore-forming fluids in magmatic-hydrothermal deposits (e.g., Rusk et al., 2004; Klemm et al., 2007; Landtwing et al., 2010; Allan et al., 2011; Appold and Wenz, 2011; Shu et al., 2017).

In this study, we provide detailed petrographic, microthermometric and LA-ICP-MS elemental data of fluid inclusions hosted in quartz grains of carbonatites in the Huangshuian Mo-(REE) deposit, the largest one in the S-NCC. This deposit contains a reserve of approximately 0.4 Mt. Mo (average grade of 0.062 wt%) with REEs as the major by-product (Li, 2014; Zhang et al., 2019). Our results characterize the physico-chemical properties of the earliest generations of the ore-forming fluids in the deposit and have important implications for regional REE mineralization associated with quartz-rich carbonatites.

2. Geological background

The S-NCC is the reactivated southernmost margin of the North China Craton and bounded by the San–Bao fault to the north and the Luanchuan fault to the south (Fig. 1). It consists of Archean to Early Paleoproterozoic basement rocks covered by Late Paleoproterozoic to Phanerozoic sequences. The basement is the widespread Taihua Group (2.84–1.97 Ga), which comprises graphite-bearing gneisses, greenstones, biotite gneisses, marbles and banded iron formations (Kröner et al., 1988; Zhang et al., 2001). The Taihua Group is unconformably overlain by the Paleoproterozoic Xiong'er Group, which is a well-preserved, unmetamorphosed volcanic sequence dominated by intermediate to acidic lavas and pyroclastic rocks with minor intercalations of clastic rocks with erupt ages of 1.78–1.45 Ga (He et al., 2009; Zhao et al., 2009). The Xiong'er Group is locally unconformably overlain by Mesoproterozoic strata which consist mainly of clastic and carbonate rocks. The above strata are intruded by Proterozoic and Mesozoic

intrusions (Fig. 1). Proterozoic intrusions are mainly alkaline granites locally distributed at the Xiaoqinling and Waifangshan regions. The Mesozoic intrusions are relatively widespread in the S-NCC and are dominated by granitic plutons and porphyry dikes, some of which are temporally and spatially associated with Mo and Au mineralization (Mao et al., 2008, 2011; Li and Pirajno, 2017).

The S-NCC hosts several carbonatite-associated deposits. Typical examples include the Huangshuian Mo-(REE) deposit in the Xiong'ershan region and the Huanglongpu Mo-(REE) and Huayangchuan U-(Nb-REE) polymetallic deposits in the Xiaoqinling region (Fig. 1). Carbonatites in these deposits consist dominantly of calcite with subordinate quartz and/or K-feldspar, remarkably distinct from typical carbonatites elsewhere (Xu et al., 2010; Song et al., 2015; Smith et al., 2018). Available geochronological data reveals that these deposits have comparable ages of mineralization at 220–200 Ma (Stein, 1997; Huang et al., 2009; Cao et al., 2014; Song et al., 2015, 2016; Zhang et al., 2019; Xue et al., 2020; Zheng et al., 2020).

3. Geology of the huanshuian Mo-(REE) deposit

The Huangshuian Mo-(REE) deposit is located at the center of the Xiong'ershan region in the S-NCC (Fig. 1). Outcropped stratum in the deposit is the Shibangou Formation of the Taihua Group which consists of biotite plagiogneiss, amphibole plagiogneiss and migmatite gneiss. Intrusive rocks include granite porphyry, quartz porphyry and the mineralization-associated carbonatites (Fig. 2). Granite porphyry is distributed at the southern section of the mining district and composed of quartz, K-feldspar, plagioclase, and biotite with accessory minerals of magnetite, zircon, titanite and ilmenite. Quartz porphyry is present as dikes and composed mainly of quartz (60%) with minor plagioclase, hornblende, and biotite. It postdates the REE mineralization as it truncates the orebodies. Carbonatites are present as plugs and dikes intruding the Taihua Group (Fig. 3a). They strike northwest with lengths of up to several kilometers. These carbonatites are generally pink in color and are composed dominantly of calcite (70%), quartz (15%) and K-feldspar (5%) with subordinate barite, celestite, biotite, fluorite, apatite, pyrite, magnetite and minor molybdenite, galena, and bastnäsite (Fig. 3b). Locally, xenoliths of the Taihua Group are observed in the carbonatites (Fig. 3c).

The Mo-REE orebodies are mainly hosted in the carbonatites and locally extend to the Taihua Group. They are generally lenticular (50–1000 m long) and strike northwest with steep dips of ~80°N. Mineralization in the deposit has a paragenetic sequence of early barren
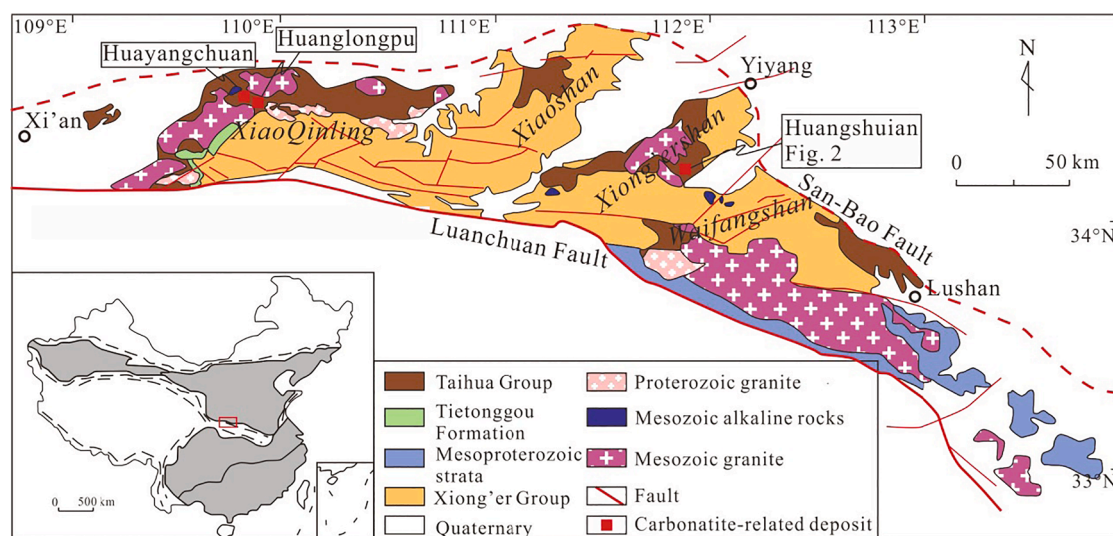

Fig. 1. Geological sketch of the Southern margin of the North China Craton (modified from Diwu et al., 2014). Also shown is the location of the Huayangchuan, Huanglongpu and Huangshuian deposits.
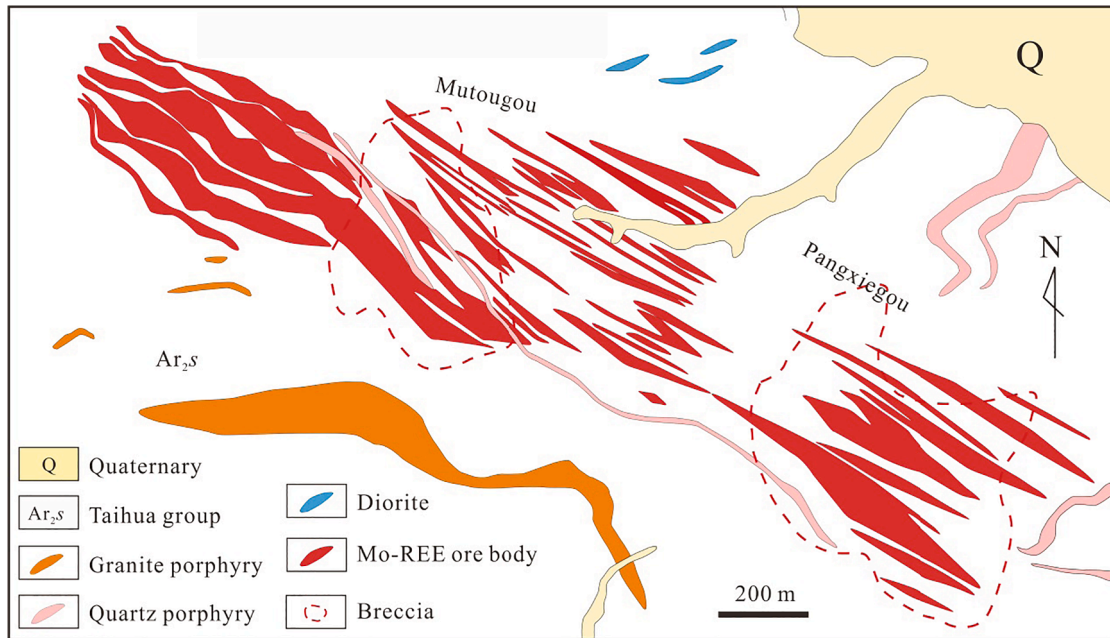
Fig. 2. Simplified geological map of the Huangshuian Mo-(REE) deposit (modified from Cao et al., 2014).
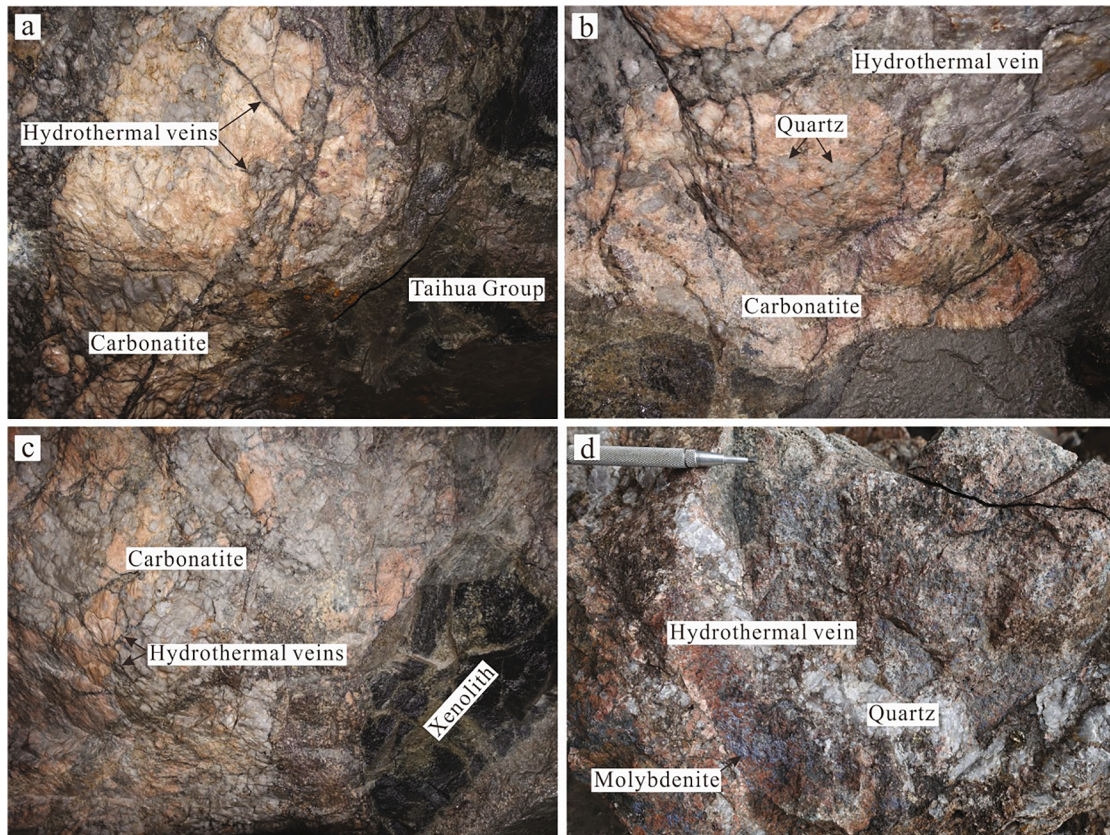

Fig. 3. Field photos of the carbonatites in the Huangshuian deposit. (a) Carbonatites occur as dikes intruding the rocks of the Taihua Group. (b) Carbonatites crosscut by later hydrothermal veins. (c) Carbonatites containing xenoliths of the Taihua Group. (d) High grade ore consists of quartz, calcite, fluorite, barite and molybdenite.

carbonatite and late hydrothermal stages. The barren carbonatite stage is characterized by disseminated bastnäsite, monazite, xenotime, and molybdenite in the carbonatites, whereas the late hydrothermal stage consists of Mo-REE-rich veins or stockworks crosscutting early carbonatites (Fig. 3d). These veins or srockworks are mostly 1 to 20 cm in thick and consist of variable amounts of quartz, calcite, barite, fluorite, apatite, pyrite, galena, sphalerite, chalcopyrite, molybdenite and REE minerals (Fig. 4a). Molybdenite occurs mainly as large patchy and small aggregates (Fig. 4a-b). The REE minerals are dominated by bastnäsite, parisite and monazite with minor allanite and xenotime (Fig. 4c-d). They
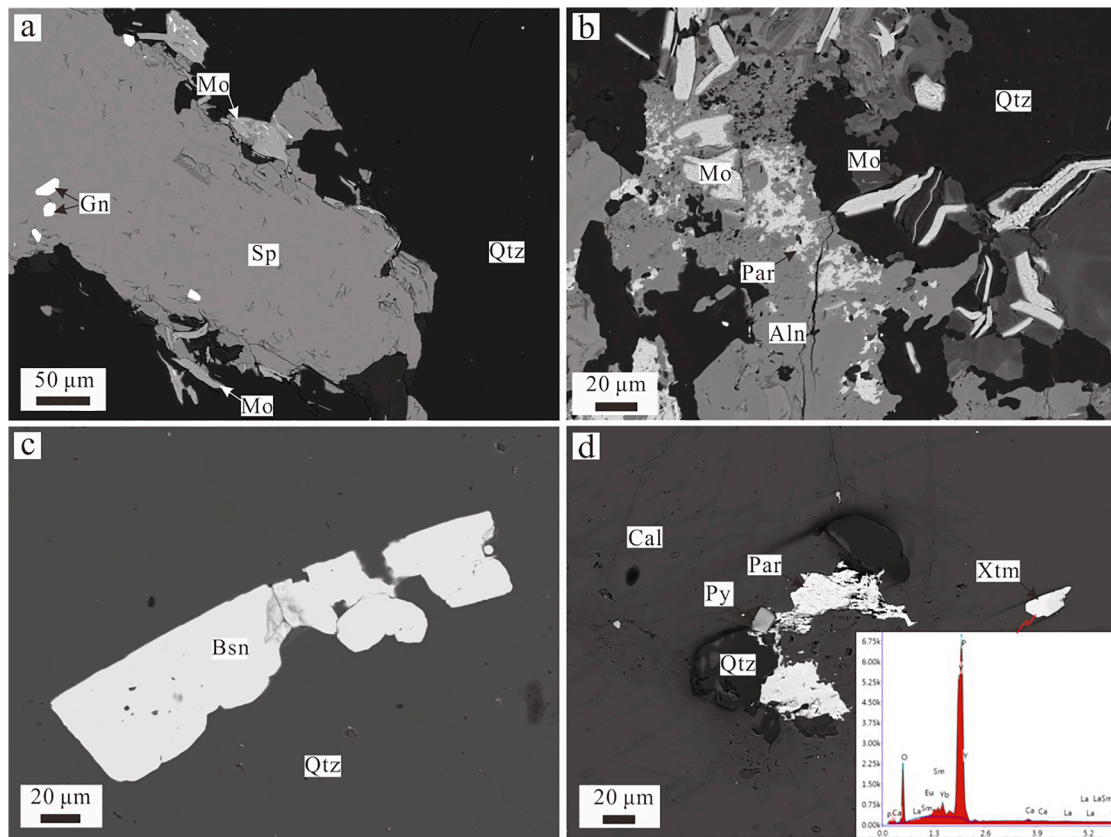
Fig. 4. Backscattered electron (BSE) images of Mo-(REE) ores in the Huangshuian deposit. (a) The intergrown galena, sphalerite and molybdenite in the hydrothermal veins. (b) The intergrown molybdenite and REE minerals (parasite and allanite) in the ores. Note that molybdenite is locally present as inclusions in the REE minerals. (c) Subhedral bastnäsite grains in the veins. (d) Xenotime in the ores. Note that the figure in the right bottom is the energy dispersive spectrometer of xenotime. Abbreviations: Gn-galena; Sp-sphalerite; Mo-molybdenite; Qtz-quartz; Par-parisite; Aln-allanite; Bsn-bastnäsite; Cal-calcite; Py-pyrite; Xtm-xenotime.

are present as subhedral to anhedral grains and generally closely associated with molybdenite (Fig. 4b). Locally, breccias are present and generally associated with Mo-(REE) mineralization. They consist of clast of carbonatites and rocks of the Taihua Group, which are cemented by hydrothermal matrix composed of quartz, calcite, barite, fluorite, pyrite, chalcopyrite, galena, molybdenite, bastnäsite, monazite, and xenotime.

4. Analytical method

4.1. Backscatter electron (BSE) and cathodoluminescence (CL) analyses

Detailed BSE and CL imaging were conducted on polished thin sections by using JSM-7800F thermal field scanning electron microscope (SEM) equipped with a TEAM Apollo XL energy disperse spectroscope and a Mono CL4 cathodoluminescence spectroscope at the State Key Laboratory of Ore Deposit Geochemistry (SKLODG), Institute of Geochemistry, Chinese Academy of Sciences, Guiyang, China. Polished thin sections were carbon-coated to avoid electrical charge build up during operation. The instruments were operated at an acceleration voltage of 15 kV, a probe current of ~10nA and a minimum magnification of 120 × when obtaining CL images of quartz.

4.2. Fluid inclusion microthermometry

Microthermometric measurements of fluid inclusions were conducted on a Linkam THMSG 600 programmable heating-freezing stage mounted on a Leica microscope at the SKLODG. Liquid nitrogen was used to freeze the fluid inclusions. The equipment permits to measure phase changes for temperatures ranging from −196 to 600 °C and was calibrated by using microthermometric behavior of synthetic fluid

inclusions of known compositions. For temperatures below 0 °C, the accuracy of the measurements is about ± 0.1 °C and for temperatures above 200 °C it is about ± 1 °C. A heating rate of 0.1 °C/s was used to obtain ice and clathrate melting temperatures. The heating rate for measurements of homogenization temperatures was 0.1 to 0.5 °C/s.

Microthermometric data of the fluid inclusion were acquired on fluid inclusion assemblages (Goldstein and Reynolds, 1994) where inclusions in a specific assemblage are supposed to display similar phase proportions and microthermometric behaviors if they were trapped coevally. Only primary inclusions showing no evidence of post-entrapment modification were analysed. All the inclusions are CO_2-bearing, and thus the salinities are determined by the final melting of CO_2 clathrate. CO_2 concentrations and density of the fluid inclusions were calculated by using the computer program ICE (Bakker, 2003).

4.3. LA-ICP-MS trace elemental analyses of fluid inclusion

After microthermometric analyses, some fluid inclusions were selected for trace elemental analyses by using the Agilent 7900 ICP-MS equipped with a GeoLasPro 193 nm ArF excimer laser at SKLODG. Details of the analytical procedure are available in Lan et al. (2017) and Lan et al. (2018), and thus are briefly summarized here. The samples were loaded along with the standard in an ablation cell on a modified petrographic microscope. The analyses were performed at energy densities of 10 J/cm^2, laser pulse frequencies of 8 Hz and spot sizes of 16 to 44 μm, depending on the sizes of the fluid inclusions. Concentrations of Li, Na, K, Mn, Fe, Cu, Zn, As, Rb, Sr, Mo, Ag, Sn, Sb, Ba, Pb and REEs including La, Ce, Pr, Nd, Yb, Lu and Y were measured in each inclusion. Quantification of single-inclusion LA-ICP-MS signals involves signal integration, background subtraction, subtraction of host-mineral

contributions, and calibration of element ratios using an external standard. After measuring a background of ~20 s, the laser was turned on and the beam diameters were stepwise increased. Once the fluid inclusions were reached and opened, the mixed signals of both the fluid inclusion and host mineral typically lasted between 5 and 15 s. Constant signals of the host mineral before or after those of fluid inclusions were used for mineral matrix correction.

Reduction of the LA-ICP-MS fluid inclusion data was carried out using the SILLS (Signal Integration for Laboratory Laser Systems) software package (Guillong et al., 2008). NIST SRM 610 was used as the external standards. The concentrations of Na in fluid inclusions, which were obtained independently through melting temperatures of last CO_2 clathrate during microthermometric analyses, were used as internal standard for calculations of elemental concentrations.

5. Results

5.1. Mineralogy of quartz in the carbonatites

Carbonatites in the Huangshuian deposit contain abundant quartz grains (Fig. 3b), similar to other carbonatites in the S-NCC (Song et al., 2015; Smith et al., 2018). These quartz grains are smoky gray in color, subhedral to anhedral in habit and hosted in calcite matrix (Fig. 5a). They contain primary mineral inclusions of calcite, K-feldspar and magnetite (Fig. 5b). In the CL images, they are generally homogeneous without internal growth zonation or secondary rim/domains, and exhibit high CL intensity with bright luminescence (Fig. 5c). Some quartz grains that are overprinted by late hydrothermal veins exhibit complex CL textures, and generally contain healed fractures and cracks that have dull CL-luminescence (Fig. 5d).

5.2. Petrography and microthermometry of fluid inclusions

Both primary and secondary fluid inclusions were observed in the quartz grains from the carbonatites of the Huangshuian deposit, and can be distinguished by using the classification of Roedder (1984). Primary inclusions are distributed in the growth zones of quartz, or presenting as isolated inclusions or as clusters concentrating in the base part of the quartz crystals without any obvious fractures. In contrast, secondary fluid inclusions are located in linear arrays along healed fractures. In this paper, only primary fluid inclusions with negative and rounded shapes were selected for microthermometric and LA-ICP-MS analyses.

Primary fluid inclusions in the quartz of carbonatites are two- and three-phase CO_2-bearing fluid inclusions (Fig. 6). These inclusions are generally irregularly distributed or occur as three-dimensional clusters (Fig. 6a). They are up to 30 μm in sizes with bubbles occupy 40–60 vol% of the inclusions. Most of these inclusions show the coexistence of liquid and gaseous CO_2 at room temperatures (Fig. 6b-c). Few inclusions also contain one or two small opaque solids but without halite (Fig. 6c).

Microthermometric results of the CO_2-bearing fluid inclusions are provided in Table 1. During cooling, the inclusions are able to be frozen and solid CO_2 were formed when the temperatures dropped to −120 °C. During heating, solid CO_2 decomposed at the temperature of about −56 °C, indicating that the CO_2 is the dominant gas in the fluid inclusions. Ice melting temperature varies from −3.1 to −5.7 °C. Clathrates were observed in all the inclusions with melting temperatures ranging from 5.0 to 7.9 °C, corresponding to salinities of 3.21 to 4.35 wt % NaCl equiv. (average at 3.88 wt% NaCl equiv) (Fig. 7a). The CO_2 concentrations of the fluid inclusions vary from 4.32 to 7.44 mol % and the fluids have calculated densities ranging from 0.54 to 0.65 g/cm³. All the inclusions are homogenized to liquids at the temperatures of 383 to 415 °C, with an average value of 396 °C (Fig. 7b).
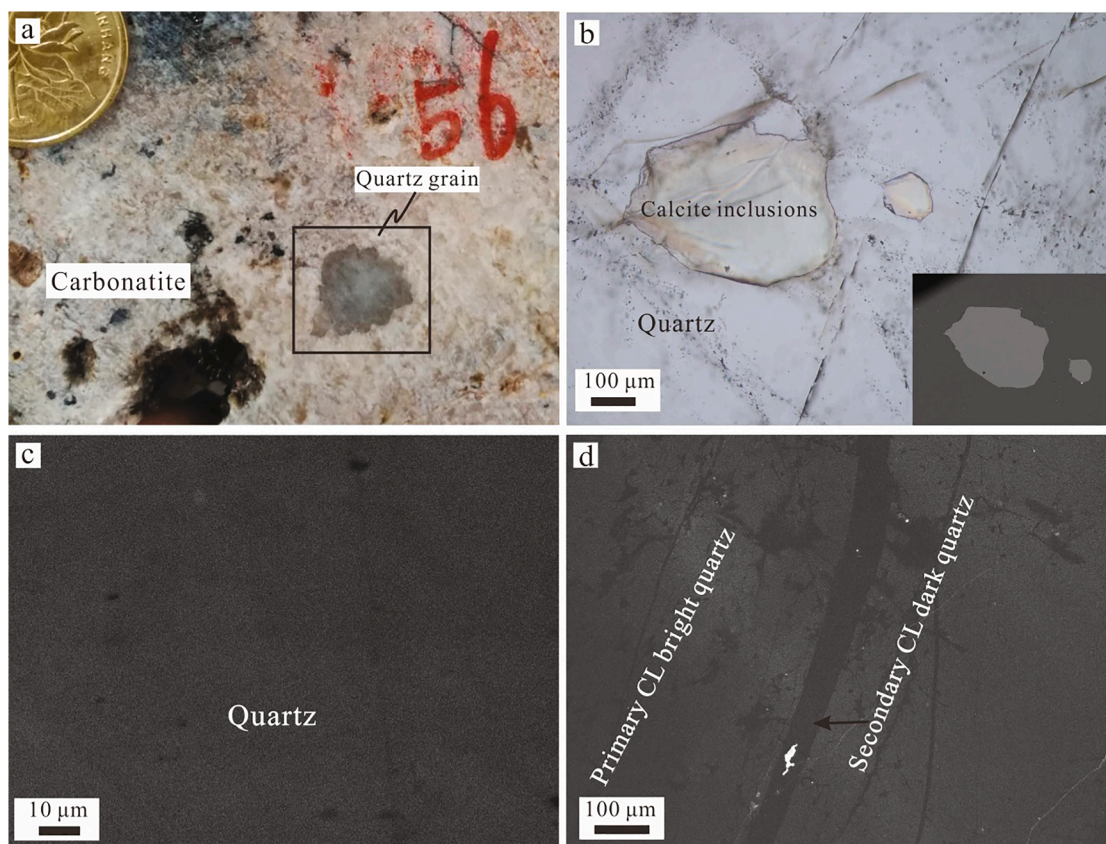

Fig. 5. (a) Subhedral quartz grains in the carbonatites. (b) Calcite inclusions in quartz from the carbonatites. Note that the figure in the right bottom is the BSE image showing calcite inclusions. (c) Quartz grains in the carbonatites showing homogeneous textures. (d) Primary quartz in the carbonatite overprinted by CL-dark quartz presenting as cracks or veinlets.
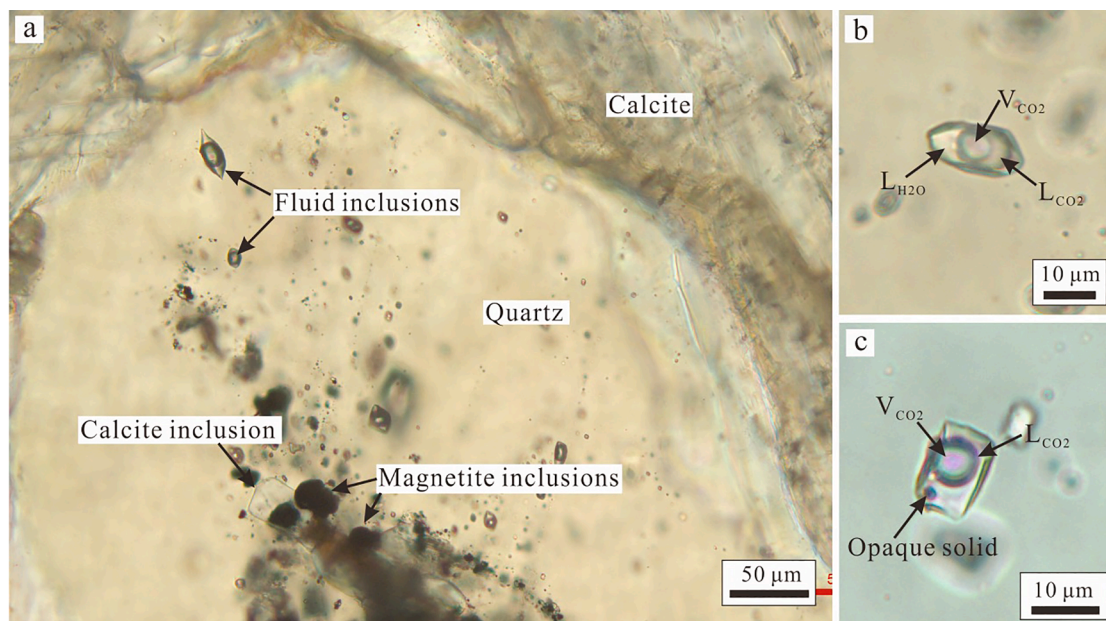
Fig. 6. Microphotographs of fluid inclusions in the primary quartz grains in the carbonatites. (a) Primary two- and three-phase CO_2-bearing fluid inclusions and mineral inclusions in quartz. (b) Three-phase CO_2-rich fluid inclusions with two bubbles (liquid and vapor CO_2). (c) Three-phase CO_2-rich fluid inclusions containing an opaque solid.

5.3. Trace elemental compositions of fluid inclusions

Elemental compositions of 21 fluid inclusions were obtained by LA-ICP-MS (Table 2). These inclusions generally contain detectable quantities of Li, Na, K, Mn, Fe, Cu, Zn, Rb, Sr, Ba, REE, and Pb whereas other elements are generally below the detection limits. The concentrations of Na and K range from 10,000 to 30,000 ppm and 1600 to 9900 ppm, respectively. Average concentrations of Rb, Sr and Ba are 40, 910 and 130 ppm, respectively. The concentrations of Cu, Pb and Zn are elevated with average values of 810, 750 and 580 ppm, respectively. Although Mo is the most important economic metal in the deposit, it is not detected in all the fluid inclusions.

The detectable REEs are presented in about half of the analyzed fluid inclusions and are dominated by LREEs (e.g., La, Ce, Pr, Nd) (Fig. 8). The concentration of La ranges from 2 to 20 ppm whereas concentration of Ce ranges from 3 to 45 ppm. Pr and Nd are occasionally detected and have concentrations ranging from 1 to 6 and 8 to 15 ppm, respectively. HREE, represented by Y, is detected in three inclusions with a highest concentration of 31 ppm.

6. Discussion

6.1. Origin of quartz in the carbonatites

Carbonatites are composed mainly of carbonates (e.g., calcite, dolomite) with variable amounts of silicates that are generally Si-unsaturated, such as olivine and nepheline. Quartz, which is Si-saturated mineral, has been traditionally considered to be exotic phase in the carbonatites (Barker, 2001). However, the occurrences of quartz have been reported in a number of carbonatites, especially those associated with REE mineralization, such as those in the Maoniuping, Montainpass, Ashram, and Montviel deposits (Mitchell, 2005; Castor, 2008; Nadeau et al., 2015; Xie et al., 2015; Mitchell and Smith, 2017). In the S-NCC, the carbonatites contain up to 20 vol% of quartz (Song et al., 2015). These quartz grains generally exhibit homogeneous CL textures without internal growth zonation or secondary rim/domains (Fig. 5c-d), and in some cases contain calcite inclusions (Fig. 6a), indicating that they are primary phases crystallized together with calcite from the evolved carbonatite melts. carbonatite melts may contain abundant

volatile components and are capable to dissolve up to 10 wt% of water (Treiman and Schedl, 1983; Keppler, 2003). As crystallization progresses, these volatile components will be saturated in the magmas and finally exsolve into a separate fluid phase (Rankin, 2005; Xie et al., 2015; Verplanck et al., 2016). Quartz is capable to crystallize from the highly evolved, fluid-saturated carbonatite melts, which is supported by the fact that the quartz grains in the carbonatites of the Huangshuian deposit contain abundant fluid inclusions (Fig. 6).

6.2. The nature of early generation of ore-forming fluids

As quartz grains in the Huangshuian carbonatites were crystallized from the fluid-saturated carbonatite melts, their captured fluid inclusions may represent the earliest generation of fluids exsolved from the magmas. Our results show that the primary CO_2-rich fluid inclusions in the quartz of the carbonatites have high homogenization temperatures (average at 396 °C) and low salinities (average at 3.88 wt% NaCl equiv). As such, the isochore of these fluid inclusions is plotted in the single-phase (supercritical) domain above the two-phase vapor–liquid boundary in the P-T phase diagram (Fig. 9), indicating that the fluids were captured in a single-phase condition. Single-phase fluids were generally identified at deep depths in magmatic-hydrothermal systems and were widely confirmed to be efficient for transporting ore components as they are highly mobile and capable to dissolve appreciable amounts of metals (e.g., Cu, Ag, Mo, and REE) by forming aqueous complexes (Norton and Dutrow, 2001; Coumou et al., 2008; Williams-Jones and Migdisov, 2014).

Our new LA-ICP-MS trace elemental analyses of fluid inclusions further reveal that the fluids recorded in the quartz of carbonatites are rich in Sr and Ba, REE, Cu, Pb, and Zn, thus indicative of a high fertility. Such a metal association is consistent with the mineral assemblages of the Huangshuian Mo- (REE) deposit, such as the widespread barite, celestite, bastnäsite, xenotime, chalcopyrite, galena, and sphalerite, thus strongly supporting that the Mo-(REE) mineralization in deposit is genetically related to the quartz-rich carbonatites. It is noteworthy that although Huangshuian is an economic Mo deposit, the concentration of Mo in the fluid inclusions is blow the detection limit of LA-ICP-MS. Similar situation is also documented in porphyry Mo deposits where Mo was not detected in the earliest high-temperature aqueous fluid

Table 1
Microthermometric results of fluid inclusions hosted in the quartz of Huangshuian carbonatites.

Sample	Bubble volume range (%)	Tm, CO$_2$ (°C)	Tm, cla (°C)	Tm, ice (°C)	Th (°C)	Salinity (wt% NaCl equiv)	Mol % of CO$_2$	Density(g/cm3)
2-1-1	50	–	5.9	−4.7	401	3.93	5.61	0.57
2-1-2	50	–	5.3	−4.6	387	4.09	5.34	0.54
2-1-3	45	−56.4	6.0	−4.2	392	4.09	5.27	0.60
2-1-4	50	−56.6	5.5	−4.6	384	4.04	5.46	0.54
2-2-1	45	−56.2	6.5	−5.2	397	3.88	5.57	0.60
2-2-2	40	−56.3	6.3	−5.0	402	4.11	4.97	0.64
2-2-3	45	−56.2	6.5	−5.3	399	3.87	5.57	0.60
2-3-1	40	−56.1	5.2	−5.7	386	4.35	4.32	0.66
2-3-2	50	−56.4	5.0	−5.8	392	4.11	5.05	0.56
2-4-1	45	−56.5	6.5	−4.5	395	3.72	6.15	0.55
2-4-2	40	−56.9	6.8	−4.2	400	4.01	5.30	0.65
2-4-3	45	–	6.6	−4.3	399	3.90	5.66	0.60
2-5-1	45	–	6.1	−4.5	394	4.04	5.33	0.60
2-5-2	40	−56.8	6.1	−4.3	391	4.21	4.87	0.64
2-5-3	45	−56.6	5.9	−4.1	390	4.12	5.21	0.59
23-1-1	50	–	6.6	−4.1	407	3.71	6.23	0.55
23-1-2	50	−56.3	6.9	−3.8	405	3.63	6.48	0.55
23-1-3	45	−56.5	6.6	−3.9	408	3.92	5.67	0.60
23-1-4	50	–	6.8	−3.9	410	3.65	6.40	0.55
23-2-1	50	–	6.9	−4.0	400	3.61	6.47	0.55
23-2-2	50	–	7.1	−3.9	397	3.53	6.65	0.56
23-2-3	50	−56.5	7.3	−3.5	392	3.48	6.84	0.56
23-2-4	50	−56.6	7.2	−3.6	394	3.52	6.75	0.56
23-2-5	45	−56.5	7.2	−3.8	387	3.72	6.13	0.60
23-3-1	45	−56.5	6.2	−4.5	395	4.01	5.39	0.60
23-3-2	40	–	6.5	−4.2	397	4.10	5.11	0.65
23-4-1	45	−56.2	5.7	−4.8	405	4.15	4.99	0.61
23-4-2	45	–	5.5	−5.1	399	4.17	4.96	0.59
23-4-3	50	–	5.9	−4.8	402	3.93	5.61	0.57
56-1-1	50	–	7.5	−3.2	403	3.41	7.04	0.56
56-1-2	45	−56.3	7.3	−3.8	399	3.68	6.21	0.61
56-1-3	50	−56.5	7.6	−3.8	398	3.34	7.12	0.56
56-1-4	45	−56.2	7.5	−3.5	395	3.62	6.39	0.61
56-2-1	45	−56.8	5.5	−4.7	398	4.19	4.97	0.59
56-2-2	45	−56.5	5.8	−4.3	401	4.15	5.06	0.62
56-2-3	40	−56.5	6.1	−4.1	399	4.22	4.87	0.64
56-2-4	45	–	5.8	−4.2	398	4.16	5.06	0.62
56-2-5	40	–	5.9	−4.3	404	4.26	4.76	0.64
56-3-1	50	−56.3	6.3	−4.3	395	3.81	6.00	0.55
56-3-2	50	–	6.0	−4.1	383	3.92	5.80	0.55
56-3-3	45	−56.2	6.1	−4.1	388	4.06	5.33	0.60
56-3-4	45	–	6.0	−4.2	390	4.09	5.27	0.60
56-3-5	50	–	6.2	−4.2	386	4.08	5.41	0.60
56-4-1	45	−56.3	7.5	−3.2	389	3.63	6.40	0.61
56-4-2	40	−56.4	7.3	−3.5	385	3.90	5.68	0.65
56-4-3	45	–	7.2	−3.6	391	3.73	6.13	0.60
56-4-4	45	−56.3	7.2	−3.5	387	3.74	6.14	0.60
56-5-1	50	−56.4	7.9	−3.2	406	3.21	7.44	0.57
56-5-2	50	−56.7	7.8	−3.1	412	3.27	7.34	0.56
56-5-3	45	–	7.8	−3.5	415	3.49	6.67	0.61
56-6-1	45	−56.3	6.0	−4.5	387	4.07	5.26	0.60
56-6-2	45	−56.2	5.9	−4.8	385	4.10	5.11	0.62
56-6-3	50	−56.5	6.2	−4.3	391	3.84	5.93	0.55
56-6-4	45	–	6.0	−4.2	390	4.09	5.27	0.60

Notes: Tm, CO$_2$ = final melting of solid CO$_2$; Tm, cla = final melting of CO$_2$ Clathrate; Tm, ice = final melting of ice in °C; Th = homogenization temperature; − = not applicable.

inclusions (e.g., Rusk, 2004; Landtwing et al., 2010). The cut-off grade of Mo is extremely low of about 0.006%. Therefore, it is quite likely that the concentration of Mo in the earliest generation of fluid is too low to be detected by LA-ICP-MS, but is able to be enriched during transportation and evolution of the exsolved fluids. For example, Mo will be highly enriched during the fluid immiscible process by preferentially partitioned into the high-salinity end-members, as evidenced by the fact that high Mo concentrations were generally identified in the high-density brine inclusions (e.g., Klemm et al., 2007; Audetat et al., 2008).

6.3. Compared to ore-forming fluids in other carbonatite-related deposits

More and more studies documented that the significant carbonatite-

related mineralization in the world occurred at late stages of carbonatite evolution involving hydrothermal fluids (e.g., Hou et al., 2009; Moore et al., 2015; Nadeau et al., 2015; Trofanenko et al., 2016; Broom-Fendley et al., 2017; Walter et al., 2020). Fluid inclusions have been widely used to constrain the nature of ore-forming fluids in carbonatite-related deposits (e.g. Rankin, 1975, 2005; Bühn and Rankin, 1999; Williams-Jones and Palmer, 2002; Prokopyev et al., 2020; Xie et al., 2009, 2015; Shu and Liu, 2019; Walter et al., 2020, 2021). Walter et al. (2021) summarized the fluid inclusions in carbonatite-related deposits and divided them into four types, including low to high density H$_2$O-NaCl fluid inclusions (Type I), low to high-density H$_2$O–(NaCl)–CO$_2$ fluid inclusions (Type II), CO$_2$-free, high-salinity, multi-phase fluid inclusions (Type III), and CO$_2$-bearing, high salinity, multi-phase fluid
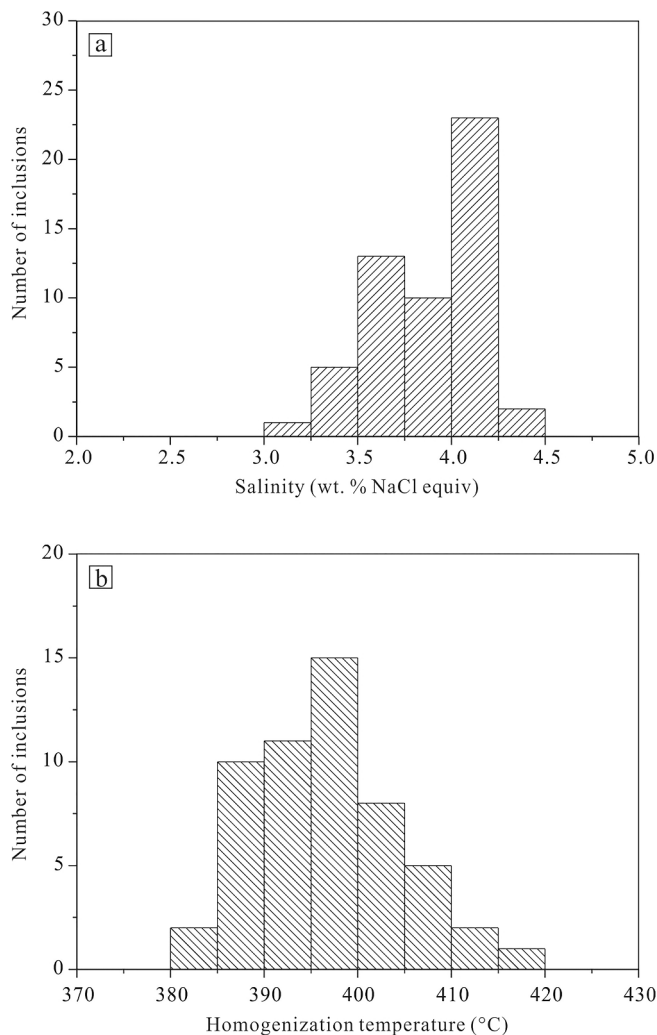
Fig. 7. Histograms showing the salinity (a) and homogenization temperature (b) of the fluid inclusions.

inclusions (Type IV). The two- and three-phase CO_2-rich fluid inclusions in the Huangshuian deposit are similar to the Type II inclusions of Walter et al. (2021). Such CO_2-rich, low salinity (<5 wt% NaCl equiv) fluid inclusions were also documented in other carbonatite-related deposits, such as Songwe Hill REE deposit in Malawi (Broom-Fendley et al., 2017), Bayan Obo Fe-REE-Nb deposit in northern China (Smith and Henderson, 2000), and Miaoya REE-Nb deposit in central China (Wu et al., 2011a, 2011b). This type of inclusions generally has high homogenization temperatures (>300 °C) and represents early stage of fluids exsolved from the carbonatite melts (Smith and Henderson, 2000; Broom-Fendley et al., 2017).

The LA-ICP-MS results of this study reveal that the earliest generation of fluids in the Huangshuian deposit is rich in light REE, Sr and Ba (Table 2), consistent with those recorded in other carbonatite-related deposits, such as Okorusu, Maoniuping, Lizhuang, and Dalucao deposits (Bühn et al., 2002; Xie et al., 2009, 2015; Shu and Liu, 2019; Zheng et al., 2021). It should be also noteworthy that some fluid
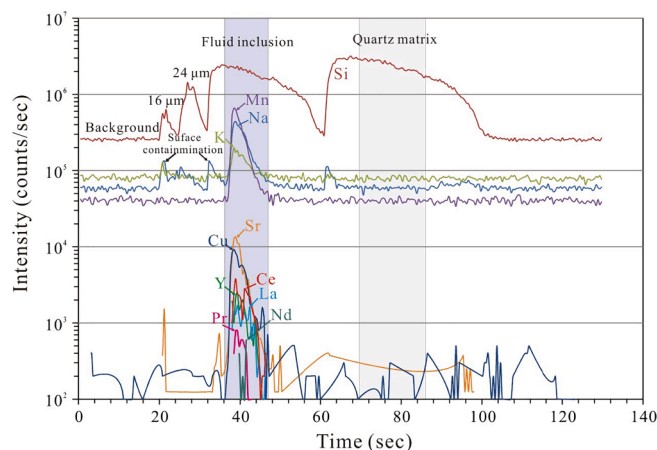

Fig. 8. Typical time-resolved LA-ICP-MS signal for selected elements (Na, Si, K, Mn, Cu, Sr, Y, La, Ce, Pr and Nd) obtained from the ablation of the two- and three-phase CO_2-bearing fluid inclusions in quartz. Note that the conspicuous signals for Na and K at the beginning of ablation are due to surface contamination.
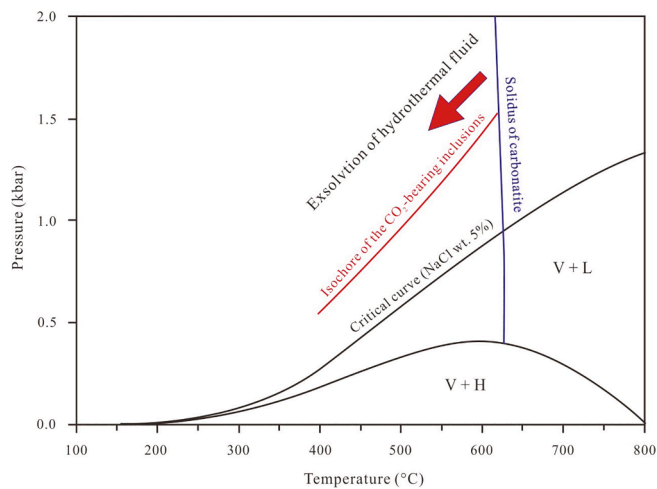
Table 2
LA-ICP-MS trace element compositions of the fluid inclusions.

Spots	Li	Na	K	Mn	Fe	Cu	Zn	Rb	Sr	Y	Mo	Ba	La	Ce	Pr	Nd	Yb	Lu	Pb
2-1-1	120	28,000	9900	540	1130	1520	130	70	340	BD	BD	75	BD	BD	BD	BD	BD	BD	1230
2-2-1	10	20,000	2200	550	70	1050	120	BD	1770	7	BD	431	19	32	4	11	BD	BD	370
2-2-3	280	23,000	7400	4140	BD	BD	BD	50	1610	BD	BD	108	6	12	1	6	BD	BD	850
2-4-3	110	15,000	4300	1140	1560	180	530	30	480	BD	BD	202	BD	BD	BD	BD	BD	BD	1790
2–5–2	160	29,000	8800	1770	1690	860	960	60	970	BD	BD	280	4	8	BD	BD	BD	BD	1560
2-5-3	220	30,000	9800	BD	BD	20	BD	50	280	BD	BD	17	BD	BD	BD	BD	BD	BD	10
23-1-2	220	24,000	7600	280	BD	430	250	90	290	BD	BD	41	BD	BD	BD	BD	BD	BD	680
23-2-1	890	16,000	3300	BD	BD	50	630	50	2140	BD	BD	26	BD	BD	BD	BD	BD	BD	210
23-2-3	70	12,000	3100	820	3720	420	430	20	1600	BD	BD	34	2	5	BD	BD	BD	BD	1880
2-3-2	BD	19,000	3200	4080	9000	BD	BD	BD	1620	BD	BD	BD	7	16	BD	BD	BD	BD	BD
2-4-3	200	11,000	5800	BD	BD	5900	BD	BD	1500	BD	BD	18	BD	BD	BD	BD	BD	BD	270
56-1-1	90	28,000	8900	7860	1570	1260	1830	40	3090	BD	BD	412	20	45	4	15	BD	BD	1030
56-1-3	BD	18,000	2400	BD	BD	BD	320	BD	240	BD	BD	75	16	44	6	15	BD	BD	450
56-1-4	190	22,000	9100	1760	BD	110	730	40	240	BD	BD	124	BD	BD	BD	BD	BD	BD	990
56-2-3	150	15,000	3600	BD	BD	470	BD	20	160	BD	BD	BD	BD	BD	BD	BD	BD	BD	BD
56-3-2	80	13,000	3600	9360	570	590	BD	20	200	31	BD	BD	21	37	6	11	BD	BD	BD
56-4-1	250	22,000	8400	BD	BD	190	770	40	250	BD	BD	321	2	4	BD	BD	BD	BD	670
56-4-5	390	22,000	9300	BD	BD	140	490	70	280	BD	BD	32	BD	BD	BD	BD	BD	BD	360
56-5-1	BD	12,000	1600	BD	BD	50	BD	20	1310	BD	BD	43	2	3	BD	BD	BD	BD	150
56-6-2	280	21,000	5100	790	720	500	340	30	360	BD	BD	26	BD	BD	BD	BD	BD	BD	270
56-5-4	240	10,000	2800	250	BD	900	BD	30	350	9	BD	3	20	36	4	8	BD	BD	BD

Notes: Detection limits varied as a function of fluid inclusion size, salinity, and instrumental sensitivity; detection limit values of specific element is as follow (ppm): Li = 2–55, Na = 29–588, K = 34–1565, Mn = 14–298, Fe = 68–1290, Cu = 2–67, Zn = 4–98, Rb = 3.1–23.4, Mo = 1.6–14.9, Sr = 0.4–15, Y = 0.4–2.7, Ba = 0.5–8.2, La = 0.4–2.3, Ce = 0.2–1.9, Pr = 0.1–1.7, Nd = 0.2–22, Pb = 0.2–4.5.

Fig. 9. Diagram of pressure verse temperature showing the formation conditions of CO_2-bearing fluid inclusions in the quartz grains of carbonatites. The isochore of fluid inclusions was calculated by using the computer program ISOC (Bakker, 2003). Pressure and temperature data of solvi is from Driesner and Heinrich (2007), while solidus of carbonatites is from Boettcher et al. (1980).

inclusions contain also considerable amounts of Y (Table 2), which was not documented in other carbonatite-related deposits. Such a feature is in agreement with local presences of xenotime in the Huangshuian deposit (Fig. 4d), thus indicating a potential of HREE mineralization which was currently poorly addressed. In addition to REEs, the earliest generation of fluids in the Huangshuian deposit is enriched in Cu, Pb, and Zn (Table 2). These base metals have also been identified in the fluids from other carbonatite-related deposits. For example, crush analyses of the bulk quartz show that the carbonatite-derived fluids in the Okorusu fluorite deposit contain 1260 ppm of Pb (Bühn et al., 2002), and LA-ICP-MS analyses of fluid inclusions in the Maoniuping REE deposit reveal that the ore-forming fluid is also enriched in Pb and Zn (Xie et al., 2015). These similar features indicate that the hydrothermal fluids exsolved from the carbonatite magmas are capable to contain abundant base metals such as Cu, Pb and Zn.

6.4. Implications for exploration

Although most Mo deposits in the S-NCC are associated with Late Mesozoic (Late Jurassic-Early Cretaceous) porphyry systems (Mao et al., 2011; Yang and Wang, 2017; Li and Pirajno, 2017), our results combined with previous studies (Xu et al., 2010; Cao et al., 2014; Song et al., 2015, 2016; Bai et al., 2019) demonstrate that the Triassic carbonatites are genetically responsible for Mo-(REE) mineralization, and thus are also important targets for Mo or REE exploration. These carbonatites are also characterized by high HREE contents and host abundant xenotime (Xu et al., 2007; Song et al., 2016; Bai et al., 2019). Although some researchers argued that the enrichments of HREEs are due to late hydrthermal overprint or remoblization (Smith et al., 2018), our new results of LA-ICP-MS analyses of fluid inclusions strongly support that the original carbonatite-derived fluids in the Huangshuian deposit are indeed rich in HREEs. Similar HREE-enriched carbonatites have also been recognized in Songwe Hill, Malawi (Broom-Fendley et al., 2017); Bear Lodge, Wyoming (Andersen et al., 2016) and Lofdal, Namibia (Wall et al., 2008), further indicating that the quartz-rich carbonatites in S-NCC should be also targets for HREE exploration. In addition to REEs, our results show that the fluids recorded in the carbonatites are Cu, Pb, and Zn-fertile (Table 2). Similar carbonatite-hosted sulfide mineralization has been also reported in literatures, such as the super-large Phalaborwa Cu deposit in the South Africa (Wu et al., 2011a, 2011b; Milani et al., 2017). We thus speculate that the quartz-rich carbonatites in S-NCC could be also potential targets for Cu, Pb, and Zn exploration.

7. Conclusion

The Huangshuian carbonatites in the S-NCC are characterized by containing abundant quartz grains and hosting economic Mo-(REE) deposit. Quartz grains in the carbonatites are hydrothermal in origin and crystallized from the highly evolved, fluid-saturated carbonatite melts. The two- and three-phase CO_2-bearing fluid inclusions in the quartz grains have high homogenization temperatures (average at 396 °C) and low salinity (average at 3.88 wt% NaCl equiv), and were captured in the single-phase (supercritical) condition. These inclusions contain high concentrations of Sr, Ba, REE, Cu, Pb, and Zn, consistent with the mineral assemblages in the deposits, thus strongly supporting that the Mo-(REE) mineralization and quartz-rich carbonatites in Huangshuian are genetically related. This new findings imply that the quartz-rich carbonatites in S-NCC could be potential targets for REE, Cu, Pb, and Zn exploration. This study further highlights that quantifying metal budgets of fluid inclusions could be a robust way to evaluate the fertility of carbonatites.

Declaration of Competing Interest

The authors declare that they have no known competing financial interests or personal relationships that could have appeared to influence the work reported in this paper.

References

Allan, M.M., Morrison, G.W., Yardley, B.W.D., 2011. Physicochemical evolution of a porphyry-breccia system: a laser ablation ICP-MS study of fluid inclusions in the mount leyshon Au deposit, Queensland, Australia. Econ. Geol. 106 (3), 413–436.

Andersen, A.K., Clark, J.G., Larson, P.B., Neill, O.K., 2016. Mineral chemistry and petrogenesis of a HFSE(+HREE) occurrence, peripheral to carbonatites of the Bear Lodge alkaline complex, Wyoming. Am. Miner. 101 (7), 1604–1623.

Appold, M.S., Wenz, Z.J., 2011. Composition of ore fluid inclusions from the viburnum trend, southeast missouri district, united states: implications for transport and precipitation mechanisms. Econ. Geol. 106 (1), 55–78.

Audetat, A., Pettke, T., Heinrich, C.A., Bodnar, R.J., 2008. Special paper: the composition of magmatic-hydrothermal fluids in barren and mineralized intrusions. Econ. Geol. 103 (5), 877–908.

Bai, T., Chen, W., Jiang, S.-Y., 2019. Evolution of the carbonatite Mo-HREE deposits in the Lesser Qinling Orogen: insights from in situ geochemical investigation of calcite and sulfate, 103069 Ore Geol. Rev. 113. https://doi.org/10.1016/j.oregeorev.2019.103069.

Bakker, R.J., 2003. Package FLUIDS 1. Computer programs for analysis of fluid inclusion data and for modlling bulk fluid properties. Chem. Geol. 194, 3–23.

Barker, D.S., 2001. Calculated silica activities in carbonatite liquids. Contrib. Mineral. Petr. 141 (6), 704–709.

Boettcher, A.L., Robertson, J.K., Wyllie, P.J., 1980. Studies in synthetic carbonatite systems: Solidus relationships for CaO-MgO-CO₂-H₂O to 40 kbar and CaO-MgO-SiO₂-CO₂-H₂O to 10 kbar. J. Geophys. Res.-Solid Earth 85 (B12), 6937–6943.

Broom-Fendley, S., Brady, A.E., Wall, F., Gunn, G., Dawes, W., 2017. REE minerals at the Songwe Hill carbonatite, Malawi: HREE-enrichment in late stage apatite. Ore Geol. Rev. 81, 23–41.

Bühn, B., Rankin, A.H., 1999. Composition of natural, volatile-rich Na-Ca-REE-Sr carbonatitic fluids trapped in fluid inclusions. Geochim. Cosmochim. Acta 63 (22), 3781–3797.

Bühn, B., Rankin, A.H., Schneider, J., Dulski, P., 2002. The nature of orthomagmatic, carbonatitic fluids precipitating REE, Sr-rich fluorite: fluid-inclusion evidence from the Okorusu fluorite deposit, Namibia. Chem. Geol. 186 (1-2), 75–98.

Cao, J., Ye, H.S., Li, H., Li, Z., Zhang, X.K., He, W., Li, C., 2014. Geological characteristics and molybdenite Re-Os isotopic dating of Huangshuian carbonatite vein-type Mo

(Pb)deposit in Songxian County, Henan Province. Mineral Deposits 33, 53–69 (in Chinese with English abstract).

Castor, S.B., 2008. The Mountain Pass rare earth carbonatite and associated ultrapotassic rocks, California. Can. Mineral. 46 (4), 779–806.

Coumou, D., Driesner, T., Heinrich, C.A., 2008. Heat transport at boiling, near-critical conditions. Geofluids 8, 208–215.

Decrée, S., Boulvais, P., Tack, L., André, L., Baele, J.-M., 2016. Fluorapatite in carbonatite-related phosphate deposits: the case of the Matongo carbonatite (Burundi). Miner. Deposita 51 (4), 453–466.

Diwu, C., Sun, Y., Zhao, Y., Lai, S., 2014. Early Paleoproterozoic (2.45–2.20 Ga) magmatic activity during the period of global magmatic shutdown: implications for the crustal evolution of the southern North China Craton. Precambr. Res. 255, 627–640.

Driesner, T., Heinrich, C.A., 2007. The system H2O-NaCl. Part I: Correlation formulae for phase relations in temperature-pressure-composition space from 0 to 1000°C, 0 to 5000 bar, and 0 to 1 XNaCl. Geochim. Cosmochim. Acta 71, 4880–4901.

Fan, H.R., Yang, K.F., Hu, F.F., Liu, S., Wang, K.Y., 2016. The giant Bayan Obo REE-Nb-Fe deposit, China: Controversy and ore genesis. Geosci. Front. 7, 335–344.

Goldstein, R.H., Reynolds, T.J., 1994. Systematics of fluid inclusions in diagenetic minerals: society of sedimentary Geology. SEPM Short Course 31, 199.

Groves, D.I., Gwalani, L.G., 2004. Preface – Special Issue: carbonatites and associated mineralization. Miner Petrol. 80, 123–126.

Guillong, M., Meier, D.L., Allan, M.M., Heinrich, C.A., Yardley, B.W.D., 2008. SILLS: A MATLAB-based program for the reduction of laser ablation ICP-MS data of homogeneous materials and inclusions. In: Mineralogical Association of Canada, Short Course Series, pp. 328–333.

He, Y., Zhao, G., Sun, M., Xia, X., 2009. SHRIMP and LA-ICP-MS zircon geochronology of the Xiong'er volcanic rocks: Implications for the Paleo-Mesoproterozoic evolution of the southern margin of the North China Craton. Precambr. Res. 168 (3-4), 213–222.

Heinrich, C.A., Pettke, T., Halter, W.E., Aigner-Torres, M., Audétat, A., Günther, D., Hattendorf, B., Bleiner, D., Guillong, M., Horn, I., 2003. Quantitative multi-element analysis of minerals, fluid and melt inclusions by laser-ablation inductively-coupled-plasma mass-spectrometry. Geochim. Cosmochim. Acta 67 (18), 3473–3497.

Hou, Z., Tian, S., Xie, Y., Yang, Z., Yuan, Z., Yin, S., Yi, L., Fei, H., Zou, T., Bai, G.e., Li, X., 2009. The Himalayan Mianning–Dechang REE belt associated with carbonatite–alkaline complexes, eastern Indo-Asian collision zone, SW China. Ore Geol. Rev. 36 (1-3), 65–89.

Huang, D.H., Hou, Z.Q., Yang, Z.M., Li, Z.Q., Xu, D.X., 2009. Geological and geochemical characteristics, metallogenetic mechanism and tectonic setting of carbonatite vein-type Mo (Pb) deposits in the East Qinling molybdenum ore belt. Acta Geol. Sin. 83, 1968–1984 (in Chinese with English abstract).

Keppler, H., 2003. Water solubility in carbonatite melts. Am. Mineral. 88 (11-12), 1822–1824.

Klemm, L.M., Pettke, T., Heinrich, C.A., Campos, E., 2007. Hydrothermal evolution of the El Teniente Deposit, Chile: porphyry Cu-Mo Ore deposition from low-salinity magmatic fluids. Econ. Geol. 102 (6), 1021–1045.

Kröner, A., Compston, W., Guo-wei, Z., An-lin, G., Todt, W., 1988. Age and tectonic setting of Late Archean greenstone-gneiss terrain in Henan Province, China, as revealed by single-grain zircon dating. Geology 16 (3), 211–215.

Lan, T.-G., Hu, R.-Z., Bi, X.-W., Mao, G.-J., Wen, B.-J., Liu, L., Chen, Y.-H., 2018. Metasomatized asthenospheric mantle contributing to the generation of Cu-Mo deposits within an intracontinental setting: a case study of the ~128 MaWangjiazhuang Cu-Mo deposit, eastern North China Craton. J. Asian Earth Sci. 160, 460–489.

Lan, T.G., Hu, R.Z., Fan, H.R., Bi, X.W., Tang, Y.W., Zhou, L., Mao, W., Chen, Y.H., 2017. In-situ analysis of major and trace elements in fluid inclusion and quartz: LA-ICP-MS method and applications to ore deposits. Acta Petrol. Sinica 33, 3239–3262 (in Chinese with English abstract).

Landtwing, M.R., Furrer, C., Redmond, P.B., Pettke, T., Guillong, M., Heinrich, C.A., 2010. The Bingham Canyon Porphyry Cu-Mo-Au Deposit. III. Zoned Copper-Gold Ore Deposition by Magmatic Vapor Expansion. Econ. Geol. 105 (1), 91–118.

Le Maitre, R.W., 2002. In: Igneous rocks: A classification and glossary of terms, second ed. Cambridge University Press, Cambridge, UK, pp. 1–236.

Li, J.H., 2014. Re-os isotopic dating of molybdenites from the Dashimengou molybdenum deposit in Songxian County, Henan Province, and its geological significance. Geol. China 41, 1364–1374 (in Chinese with English abstract).

Li, N., Pirajno, F., 2017. Early Mesozoic Mo mineralization in the Qinling Orogen: an overview. Ore Geol. Rev. 81, 431–450.

Mao, J.W., Pirajno, F., Xiang, J.F., Gao, J.J., Ye, H.S., Li, Y.F., Guo, B.J., 2011. Mesozoic molybdenum deposits in the east Qinling-Dabie orogenic belt: characteristics and tectonic settings. Ore Geol. Rev. 43 (1), 264–293.

Mao, J.W., Xie, G.Q., Bierlein, F., Qü, W.J., Du, A.D., Ye, H.S., Pirajno, F., Li, H.M., Guo, B.J., Li, Y.F., Yang, Z.Q., 2008. Tectonic implications from Re–Os dating of Mesozoic molybdenum deposits in the East Qinling-Dabie orogenic belt. Geochim. Cosmochim. Acta 72 (18), 4607–4626.

Milani, L., Bolhar, R., Cawthorn, R.G., Frei, D., 2017. In situ LA–ICP-MS and EPMA trace element characterization of Fe–Ti oxides from the phoscorite–carbonatite association at Phalaborwa, South Africa. Miner. Deposita 52 (5), 747–768.

Mitchell, R.H., 2005. Carbonatites and carbonatites and carbonatites. Can. Mineral. 43 (6), 2049–2068.

Mitchell, R.H., Smith, D.L., 2017. Geology and Mineralogy of the Ashram Zone Carbonatite, Eldor Complex, Québec. Ore Geol. Rev. 86, 784–806.

Moore, M., Chakhmouradian, A.R., Mariano, A.N., Sidhu, R., 2015. Evolution of rare-earth mineralization in the Bear Lodge carbonatite, Wyoming: mineralogical and isotopic evidence. Ore Geol. Rev. 64, 499–521.

Nadeau, O., Cayer, A., Pelletier, M., Stevenson, R., Jébrak, M., 2015. The Paleoproterozoic Montviel carbonatite-hosted REE–Nb deposit, Abitibi, Canada: geology, mineralogy, geochemistry and genesis. Ore Geol. Rev. 67, 314–335.

Norton, D.L., Dutrow, B.L., 2001. Complex behavior of magma-hydrothermal processes: role of supercritical fluid. Geochim. Cosmochim. Acta 65 (21), 4009–4017.

Palmer, D.A.S., Williams-Jones, A.E., 1996. Genesis of the carbonatite-host fluorite deposit at Amba Gongar, India: evidence from fluid inclusions, stable isotopes, and whole rock mineral geochemistry. Econ. Geol. 91, 934–950.

Pettke, T., Oberli, F., Audétat, A., Guillong, M., Simon, A.C., Hanley, J.J., Klemm, L.M., 2012. Recent developments in element concentration and isotope ratio analysis of individual fluid inclusions by laser ablation single and multiple collector ICP-MS. Ore Geol. Rev. 44, 10–38.

Prokopyev, I., Kozlov, E., Fomina, E., Doroshkevich, A., Dyomkin, M., 2020. Mineralogy and fluid regime of formation of the REE-late-stage hydrothermal mineralization of Petyayan-Vara carbonatites (Vuoriyarvi, Kola Region, NW Russia). Minerals 10, 405. https://doi.org/10.3390/min10050405.

Rankin, A.H., 1975. Fluid inclusion studies in apatite from carbonatites of the Wasaki area of western Kenya. Lithos 8 (2), 123–136.

Rankin, A.H., 2005. Carbonatite-associated rare metal deposits: composition and evolution of ore-forming fluids-the fluid inclusion evidence. In: Geological Association of Canada, Short Course Notes, pp. 299–314.

Roedder, E., 1984. Fluid inclusions. Rev. Mineral. 12, 1–646.

Rusk, B.G., Reed, M.H., Dilles, J.H., Klemm, L.M., Heinrich, C.A., 2004. Compositions of magmatic hydrothermal fluids determined by LA-ICP-MS of fluid inclusions from the porphyry copper–molybdenum deposit at Butte, MT. Chem. Geol. 210 (1-4), 173–199.

Shu, Q., Chang, Z., Hammerli, J., Lai, Y., Huizenga, J.M., 2017. Composition and evolution of fluids forming the Baiyinnuo'er Zn-Pb skarn deposit, Northeastern China: Insights from Laser Ablation ICP-MS study of fluid inclusions. Econ. Geol. 112, 1441–1460.

Shu, X., Liu, Y., 2019. Fluid inclusion constraints on the hydrothermal evolution of the Dalucao carbonatite-related REE deposit, Sichuan Province, China. Ore Geol. Rev. 107, 41–57.

Simandl, G.J., Paradis, S., 2018. Carbonatites: related ore deposits, resources, footprint, and exploration methods. Appl. Earth Sci. 127 (4), 123–152.

Smith, M., Kynicky, J., Xu, C., Song, W., Spratt, J., Jeffries, T., Brtnicky, M., Kopriva, A., Cangelosi, D., 2018. The Origin of secondary heavy Rare Earth Element enrichment in carbonatites: constraints from the evolution of the Huanglongpu district, China. Lithos 308-309, 65–82.

Smith, M.P., Henderson, P., 2000. Preliminary fluid inclusion constraints on fluid evolution in the Bayan Obo Fe-REE-Nb deposit, Inner Mongolia, China. Econ. Geol. 1371–1388.

Song, W., Xu, C., Qi, L., Zhou, L.i., Wang, L., Kynicky, J., 2015. Genesis of Si-rich carbonatites in Huanglongpu Mo deposit, Lesser Qinling orogen, China and significance for Mo mineralization. Ore Geol. Rev. 64, 756–765.

Song, W., Xu, C., Smith, M.P., Kynicky, J., Huang, K., Wei, C., Zhou, L., Shu, Q., 2016. Origin of unusual HREE-Mo-rich carbonatites in the Qinling orogeny, China. Sci. Rep. 6, 373–377.

Stein, H., 1997. Highly precise and accurate Re-Os ages for molybdenite from the East Qinling molybdenum belt, Shaanxi Province, China. Econ. Geol. 92, 827–835.

Treiman, A.H., Schedl, A., 1983. Properties of carbonatite magma and processes in carbonatite magma chambers. J. Geol. 91 (4), 437–447.

Trofanenko, J., Williams-Jones, A.E., Simandl, G.J., Migdisov, A.A., 2016. The nature and origin of the REE mineralization in the Wicheeda carbonatite, British Columbia, Canada. Econ. Geol. 111 (1), 199–223.

Verplanck, P.L., Mariano, A.N., Mariano, A., 2016. Rare earth element ore geology of carbonatites. In: Verplanck, P.L., Hitzman, M.W. (Eds.), Rare earth and critical elements in ore deposits. Reviews in Economic Geology, pp. 5–32.

Wall, F., Niku-Paavola, V.N., Storey, C., Muller, A., Jeffries, T., 2008. Xenotime-(Y) from carbonatite dykes at Lofdal, Namibia: unusually low LREE: HREE ratio in carbonatite, and the first dating of xenotime overgrowths on zircon. Can. Mineral. 46 (4), 861–877.

Walter, B.F., Giebel, R.J., Steele-Macinnis, M., Marks, M.A.W., Kolb, J., Markl, G., 2021. Fluid associated with carbonatitic magmatism: a critical review and implications for carbonatite magma ascent. Earth-Sci. Rev. 215, 103509.

Walter, B.F., Steele-MacInnis, M., Giebel, R.J., Marks, M.A.W., Markl, G., 2020. Complex carbonate-sulfate brines in fluid inclusions from carbonatites: estimating compositions in the system H2O-Na-K-CO3-SO4-Cl. Geochim. Cosmochim. Acta 277, 224–242.

Williams-Jones, A.E., Migdisov, A.A., 2014. Experimental constraints on the transport and deposition of metals in ore-forming hydrothermal systems. Econ. Geol. 18, 77–95.

Williams-Jones, A.E., Palmer, D.A.S., 2002. The evolution of aqueous-carbonic fluids in the Amba Dongar barbonatite, India: implications for fenitisation. Chem. Geol. 185, 283–301.

Wu, F.-Y., Yang, Y.-H., Li, Q.-L., Mitchell, R.H., Dawson, J.B., Brandl, G., Yuhara, M., 2011a. In situ determination of U-Pb ages and Sr–Nd–Hf isotopic constraints on the petrogenesis of the Phalaborwa carbonatite Complex, South Africa. Lithos 127 (1-2), 309–322.

Wu, M., Xu, C., Wang, L.J., Song, W.L., 2011b. A preliminary study on genesis of REE deposit in Miaoya. Acta Mineral. Sinica 31, 478–484 (in Chinese with English abstract).

Xie, Y., Hou, Z., Yin, S., Dominy, S.C., Xu, J., Tian, S., Xu, W., 2009. Continuous carbonatitic melt-fluid evolution of a REE mineralization system: evidence from inclusions in the Maoniuping REE deposit, Western Sichuan, China. Ore Geol. Rev. 36 (1-3), 90–105.

Xie, Y., Li, Y., Hou, Z., Cooke, D.R., Danyushevsky, L., Dominy, S.C., Yin, S., 2015. A model for carbonatite hosted REE mineralisation — the Mianning–Dechang REE belt, Western Sichuan Province, China. Ore Geol. Rev. 70, 595–612.

Xu, C., Campbell, I.H., Allen, C.M., Huang, Z., Qi, L., Zhang, H., Zhang, G., 2007. Flat rare earth element patterns as an indicator of cumulate processes in the Lesser Qinling carbonatites, China. Lithos 95 (3-4), 267–278.

Xu, C., Kynicky, J., Chakhmouradian, A.R., Qi, L., Song, W., 2010. A unique Mo deposit associated with carbonatites in the Qinling orogenic belt, central China. Lithos 118 (1-2), 50–60.

Xu, C., Taylor, R.N., Kynicky, J., Chakhmouradian, A.R., Song, W., Wang, L., 2011. The origin of enriched mantle beneath North China block: evidence from young carbonatites. Lithos 127 (1-2), 1–9.

Xue, S., Ling, M.X., Liu, Y.L., Sun, W.D., 2020. The formation of the giant Huayangchuan U-Nb deposit associated with carbonatite in the Qingling Orogenic Belt. Ore Geol. Rev. 122.

Yang, K.-F., Fan, H.-R., Santosh, M., Hu, F.-F., Wang, K.-Y., 2011. Mesoproterozoic carbonatitic magmatism in the Bayan Obo deposit, Inner Mongolia, North China: constraints for the mechanism of super accumulation of rare earth elements. Ore Geol. Rev. 40 (1), 122–131.

Yang, Y.-F., Wang, P., 2017. Geology, geochemistry and tectonic settings of molybdenum deposits in Southwest China: a review. Ore Geol. Rev. 81, 965–995.

Zhang, G.W., Zhang, B.R., Yuan, X.C., Xiao, Q.H., 2001. In: Qinling Orogenic Belt and Continental Dynamics. Science Press, Beijing, pp. 1–806 (in Chinese).

Zhang, W., Chen, W.T., Gao, J.-F., Chen, H.-K., Li, J.-H., 2019. Two episodes of REE mineralization in the Qinling Orogenic Belt, Central China: in-situ U-Th-Pb dating of bastnäsite and monazite. Miner. Deposita 54 (8), 1265–1280.

Zhao, G., He, Y., Sun, M., 2009. The Xiong'er volcanic belt at the southern margin of the North China Craton: petrographic and geochemical evidence for its outboard position in the Paleo-Mesoproterozoic Columbia Supercontinent. Gondwana Res. 16 (2), 170–181.

Zheng, H., Chen, H.Y., Li, D.F., Wu, C., Chen, X., Lai, C.K., 2020. Timing of carbonatite-hosted U-polymetallic mineralization in the supergiant Huayangchuan deposit, Qinling Orogen: constraints from the titanite U-Pb and molybdenite Re-Os dating. Geosci. Front. 11, 1581–1592.

Zheng, X., Liu, Y., Zhang, L., 2021. The role of sulfate-, alkali-, and halogen-rich fluids in mobilization and mineralization of rare earth elements: insights from bulk fluid compositions in the Mianning–Dechang carbonatite-related REE belt, southwestern China. Lithos s386-387, 106008.